Numerical investigation to the effect of initial guess for phase-field models

Sungha Yoon[1], Jian Wang[2], Chaeyoung Lee[1], Junxiang Yang[1],
Jintae Park[1], Hyundong Kim[1], Junseok Kim[1,*]

[1] *Department of Mathematics, Korea University, Seoul 02841, Republic of Korea*
[2] *School of Mathematics and Statistics, Nanjing University of Information Science and Technology, Nanjing, 210044, China*

Abstract. In this paper, we conduct a review and investigation of the necessity of adequate initial conditions for the phase-field models. Phase-field models are originally developed for solving interfacial problems implicitly. In the case of assuming a locally equilibrium state at the interface in actual physical phenomena, it should be based on the local distance function. However, a non-uniform boundary occurs in the Cartesian coordinates system. Therefore, the initial conditions must be reinitialized to match the actual phenomena to correct this problem. Moreover, we further present the volume correction method, image initialization, non-overlapping multi component concentration, etc. The methods presented in this paper are useful to construct the initial guess for various phase-field models.

1. Introduction

A phase-field model is a mathematical model for solving interfacial problems and was first introduced in [22, 33]. Examples are dendritic growth [30, 55], spinodal decomposition [38], micro-phase pattern formation [14, 58], image inpainting [5], image segmentation [52], vesicle dynamics [39, 49], tumor growth [15, 37], two-phase flow [1, 32], and multi-phase fluid flow [3, 21, 56]. In the phase-field model, we substitute boundary conditions at the interface by the phase-field equation. The phase-field function takes distinct values in each of the phases and has a smooth interfacial transition layer between distinct values. We define the interface as a contour in the two-dimensional space or an isosurface in the three-dimensional space. In the limit of an infinitesimal interfacial parameter, we can have the correct interfacial dynamics. Therefore, we can solve the interfacial related problems just by solving the equation on

---

the whole domain instead of the explicit treatment of the boundary conditions at the interface.

The first example of the phase-field equations is the Allen–Cahn (AC) equation [2] which governs the motion of anti-phase boundaries in crystalline solids

$$\frac{\partial \phi}{\partial t}(\mathbf{x}, t) = -\frac{F'(\phi(\mathbf{x}, t))}{\epsilon^2} + \Delta \phi(\mathbf{x}, t), \quad \mathbf{x} \in \Omega, \ t > 0,$$

where Ω is a domain, ϕ is the difference of concentrations, $F(\phi) = 0.25(\phi^2 - 1)^2$, and ϵ is a positive parameter related to the interfacial thickness. Figure 1 shows temporal evolutions of the contour and isosurface of the numerical solutions of the AC equations with initial conditions described in [36].
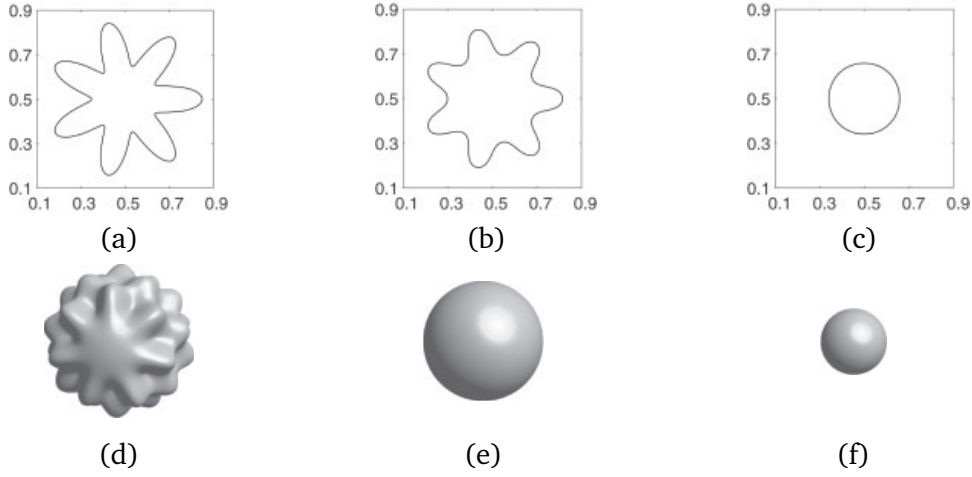

Figure 1: Motion by mean curvature. (a)–(c) and (d)–(f) show the results in two- and three-dimensional spaces, respectively. Reprinted from Li et al. [36] with permission of Elsevier Science.

Next example is the dendritic growth equations with four-fold symmetry in the two-dimensional space [30, 55]:

$$\epsilon^2(\phi)\frac{\partial \phi}{\partial t} = \nabla \cdot (\epsilon^2(\phi)\nabla\phi) + [\phi - \lambda U(1 - \phi^2)](1 - \phi^2)$$
$$+ \left(|\nabla\phi|^2 \epsilon(\phi) \frac{\partial \epsilon(\phi)}{\partial \phi_x} \right)_x + \left(|\nabla\phi|^2 \epsilon(\phi) \frac{\partial \epsilon(\phi)}{\partial \phi_y} \right)_y,$$
$$\frac{\partial U}{\partial t} = D\Delta U + \frac{1}{2}\frac{\partial \phi}{\partial t}, \quad \text{for } \mathbf{x} \in \Omega, \ t > 0,$$
$$\epsilon(\phi) = W_0 \left(1 - 3\delta_4 + 4\delta_4 \frac{\phi_x^4 + \phi_y^4}{|\nabla\phi|^4} \right),$$

where Ω is a domain, an order parameter $\phi(\mathbf{x}, t)$ takes values between -1 (liquid phase) and 1 (solid phase), W_0 is a measure of the interface width, $\epsilon(\phi)$ is the anisotropic function, and δ_4 is the anisotropic strength. λ is the dimensionless coupling parameter,

D is the diffusion rate of the temperature and $U(\mathbf{x}, t)$ is the dimensionless temperature field. Figure 2 illustrates the temporal evolution of dendritic growth in two-dimensional space.
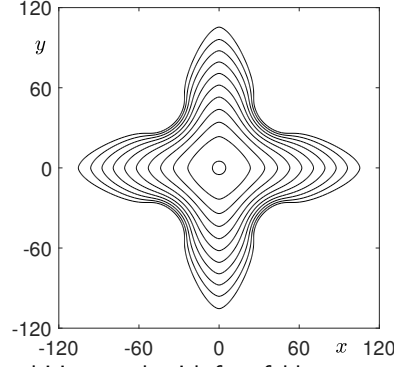

Figure 2: Temporal evolution of dendritic growth with four-fold symmetry in 2D. Reprinted from Jeong and Kim [30] with permission from Elsevier Science.

The three-dimensional dendritic growth model is given as

$$\epsilon^2(\phi)\frac{\partial \phi}{\partial t} = \nabla \cdot (\epsilon^2(\phi)\nabla\phi) + [\phi - \lambda U(1-\phi^2)](1-\phi^2)$$
$$+ \left(|\nabla\phi|^2\epsilon(\phi)\frac{\partial\epsilon(\phi)}{\partial\phi_x}\right)_x + \left(|\nabla\phi|^2\epsilon(\phi)\frac{\partial\epsilon(\phi)}{\partial\phi_y}\right)_y + \left(|\nabla\phi|^2\epsilon(\phi)\frac{\partial\epsilon(\phi)}{\partial\phi_z}\right)_z,$$
$$\frac{\partial U}{\partial t} = D\Delta U + \frac{1}{2}\frac{\partial\phi}{\partial t},$$
$$\epsilon(\phi) = W_0\left(1 - 3\delta_4 + 4\delta_4\frac{\phi_x^4 + \phi_y^4 + \phi_z^4}{|\nabla\phi|^4}\right).$$

Figure 3 illustrates the temporal evolution of dendritic growth in three-dimensional space.
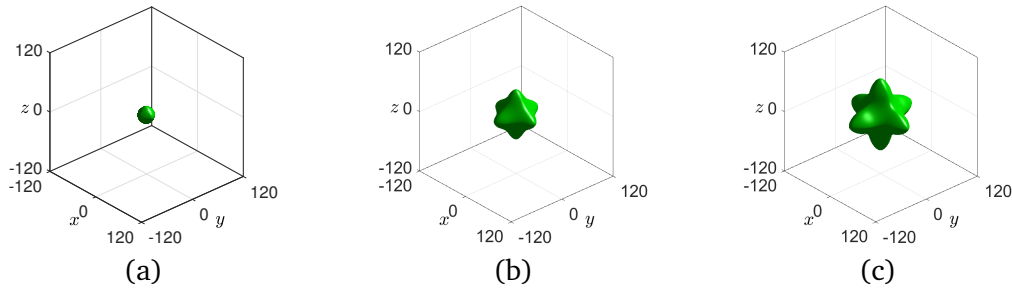

(a)   (b)   (c)

Figure 3: Temporal evolution of dendritic growth in 3D. Reprinted from Jeong and Kim [30] with permission of Elsevier Science.

Another representative example of the phase-field models is the Cahn–Hilliard (CH)

equation [7, 8]:

$$\frac{\partial \phi(\mathbf{x}, t)}{\partial t} = \Delta \mu(\mathbf{x}, t), \ \ \mathbf{x} \in \Omega, \ t > 0,$$
$$\mu(\mathbf{x}, t) = F'(\phi(\mathbf{x}, t)) - \epsilon^2 \Delta \phi(\mathbf{x}, t),$$

where $\Omega \subset \mathbb{R}^d$ ($d = 1, 2, 3$) is a domain, $F(\phi) = 0.25(\phi^2 - 1)^2$ is a double well potential energy, and ϵ is a positive parameter. The phase field $\phi(\mathbf{x}, t)$ which ranges between -1 and 1 is defined as the difference between the mole fractions of binary mixtures. As a typical example of the phase-field models, the CH equation has been widely studied in various fields of scientific research. Because both the AC and CH equations are closely related to each other, many related researches are being continuously conducted [10–12]. The CH equation with random initial condition is widely used to simulate the spinodal decomposition. Figure 4(a)–(c) and Fig. 4(d)–(f) show the evolutions of binary and multi-component spinodal decomposition [48, 53], respectively.
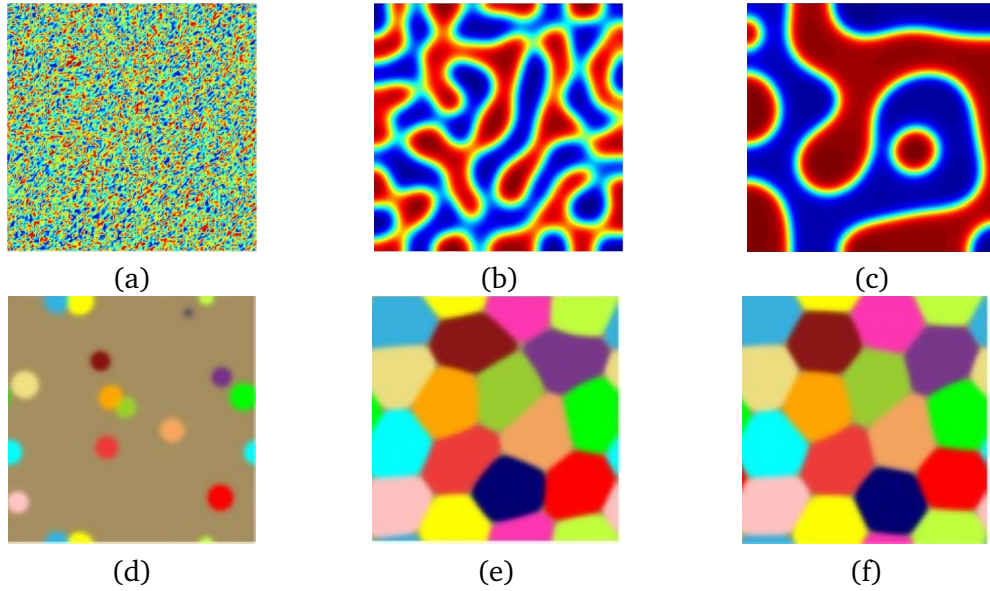

Figure 4: Temporal evolution of spinodal decomposition. (a)–(c) and (d)–(f) show the results for binary and multi-component spinodal decomposition, respectively. Adapted from [53] and [48] with permission of Elsevier Science.

Furthermore, the CH equation with a specific initial condition: $\phi(\mathbf{x}, 0) = 2(x - 0.5)$ can be used to simulate the spinodal decomposition and nucleation taking place simultaneously. Fig. 5(a)–(d) show the temporal evolutions of spinodal decomposition and nucleation in a unit domain [26].

Many important problems in the field of materials science and thin film technologies are related to open curve or surface evolution problems. One of extensively studied topics is solid-state dewetting [60–63], which has been observed in a broad area of systems and is received significant technical attention. The dewetting phenomenon is
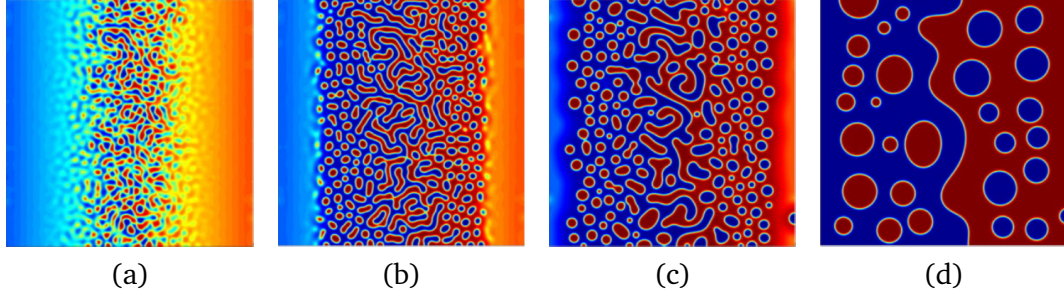
Figure 5: Temporal evolutions of spinodal decomposition and nucleation. Adapted from [26] with permission of Elsevier Science.

associated with a more generic category of capillarity-controlled interface or surface evolutions. The dewetting process is mathematically modeled and studied by applying the sharp-interface method or the phase-field method. A schematic evolution process of the solid-state dewetting of a thin film on a substrate can be seen in Fig. 6. The initial state is shown in Fig. 6(a), the intermediate state is presented in Fig. 6(b), and then the final profile of pinch-off state can be seen in Fig. 6(c). The evolution is modelled by the CH equation.
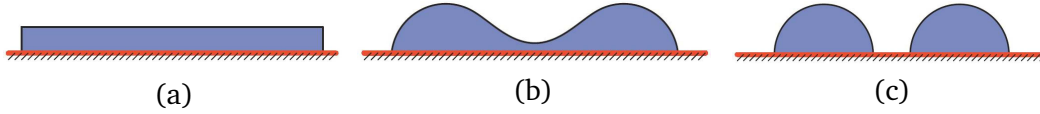

Figure 6: The solid-state dewetting of a thin film on a substrate. Reprinted from Jiang et al. [60] with permission of Elsevier Science.

Next, there is the following governing equation of diblock copolymer [14]:

$$\frac{\partial \phi(\mathbf{x}, t)}{\partial t} = \Delta \mu(\mathbf{x}, t) - \alpha(\phi(\mathbf{x}, t) - \bar{\phi}(\mathbf{x}, t)),$$
$$\mu(\mathbf{x}, t) = F'(\phi(\mathbf{x}, t)) - \epsilon^2 \Delta \phi(\mathbf{x}, t),$$

where $\bar{\phi}(\mathbf{x}, t) = \frac{1}{\Omega} \int_\Omega \phi(\mathbf{x}, t) d\mathbf{x}$. Fig. 7(a) and (b) show the snapshots of the results of diblock copolymer simulation with random initial condition around $\bar{\phi} = 0$ and $\bar{\phi} = 0.3$, respectively.

Furthermore, the Swift–Hohenberg (SH) equation is as followed [46]:

$$\frac{\partial \phi(\mathbf{x}, t)}{\partial t} = \epsilon \phi(\mathbf{x}, t) - (\Delta + 1)^2 \phi(\mathbf{x}, t) + g\phi^2(\mathbf{x}, t) - \phi^3(\mathbf{x}, t), \ \mathbf{x} \in \Omega, \ t > 0$$

with periodic boundary condition and random initial condition. It has a variety of applications such as cellular materials, crystallography, metallurgy, etc [24]. Figure 8 shows two snapshots of the numerical solutions with random initial condition. The phase-field model mainly deals with binary phase separation, and random initial conditions are often used. Even though the random initial conditions are given, as shown in Fig. 8, can be seen to evolve into any shape by solving the equation.

(a)   (b)

Figure 7: (a) and (b) are the snapshots of the results of diblock copolymer simulation with random initial condition around $\bar{\phi} = 0$ and $\bar{\phi} = 0.3$, respectively. Adapted from [14] with permission of Elsevier Science.

(a)   (b)

Figure 8: Snapshots of the numerical solutions of the Swift–Hohenberg equation with random initial conditions. Reprinted from [18] with permission of Elsevier Science.

Now, the following phase-field crystal equation is also introduced [40]:

$$\frac{\partial \phi(\mathbf{x}, t)}{\partial t} = \Delta \left[\phi^3(\mathbf{x}, t) + (1 - \epsilon)\phi(\mathbf{x}, t) + 2\Delta\phi(\mathbf{x}, t) + \Delta^2\phi(\mathbf{x}, t) \right].$$

The phase-field crystal equation has various applications, for instance, isotropic phase separation, crystallization in undercooled liquid-liquid interface, and so on. There are several theoretical papers concerning this topic [41, 42] and related numerical methods have been proposed such as operator splitting method [43], convex splitting method [44], spectral method [45], etc. Figure 9 shows the evolution of phase field crystal equation with a randomly distributed initial value in the two- and the three-dimensional spaces.
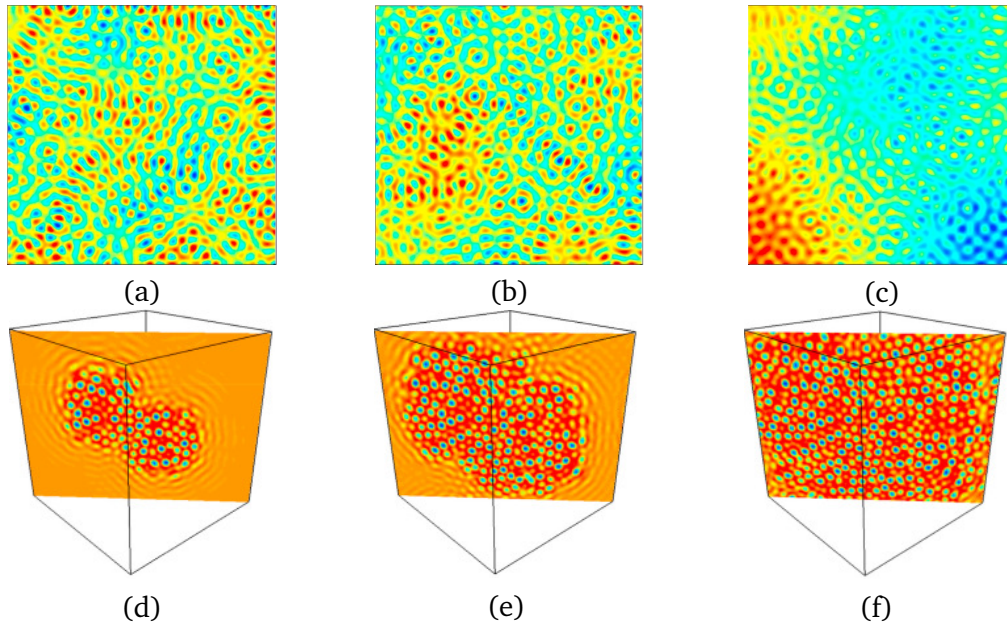

Figure 9: (a)–(c) are temporal evolutions of phase field crystal in the two-dimensional space and (d)–(f) are those of three-dimensional space in slice view. The first and second rows are reprinted from [18, 40], respectively, with permissions of Elsevier Science.

In the field of computational fluid dynamics, the Cahn–Hilliard–Navier–Stokes (CHNS) model has been used to model various two-phase flow phenomena [27]. The most typical benchmark problem for the CHNS model with variable density is the well-known Rayleigh–Taylor (RT) instability. We can take the initial condition of the CH equation as a cosine function with small amplitude, then the interfacial instability evolves with time to form the RT instability. Figure 10 shows the temporal evolution of the RT instability [47].

There have been many analytic and experimental studies on the deformation of biological vesicle membranes using a phase-field approach [39, 49]. The governing
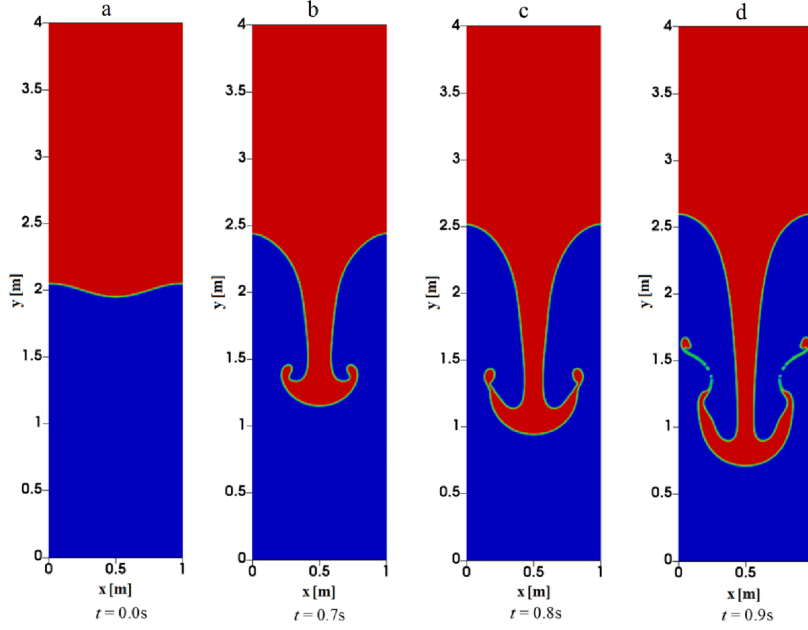
Figure 10: Temporal evolution of the RT instability. Adapted from [47] with permission of Elsevier Science.

equation derived from the elastic bending energy is given as

$$\frac{\partial \phi}{\partial t}(\mathbf{x}, t) = -g(\phi(\mathbf{x}, t)) - 2M(B(\phi(\mathbf{x}, t)) - \beta)f(\phi(\mathbf{x}, t)) + \gamma(t)F(\phi(\mathbf{x}, t)),$$

where M is a large penalty constant, $g(\phi) = \delta W(\phi)/\delta\phi$, and $f(\phi) = \delta B(\phi)/\delta\phi$. Here, $W(\phi)$ is the bending surface energy, $B(\phi)$ is the surface area. A space-time dependent Lagrange multiplier $\gamma(t)F(\phi)$ for the volume constraints is used. $F(\phi)$ and $\gamma(t)$ are defined as follows:

$$F(\phi) = \frac{(\phi^2 - 1)^2}{4} = \frac{\epsilon^2}{2}|\nabla\phi|^2,$$
$$\gamma(t) = \frac{\int_\Omega [g(\phi) + 2M(B(\phi) - \beta)f(\phi)]\, d\mathbf{x}}{\int_\Omega F(\phi)\, d\mathbf{x}}.$$

Figure 11 illustrates the temporal evolution of the vesicle membrane in three-dimensional space.

The main purpose of this paper is to present constructive initial guess for the phase-field equations. Since many researchers have difficulty setting up initial states appropriately for each experiment, we gather and explain various initial conditions. We present the algorithms based on level set approach with signed distance field [6, 9] that make more suitable and correct initial guess for the phase-field models.

The layout of this paper is organized as follows. The various initial conditions are described in Sec. 2. Conclusions are made in Sec. 3.
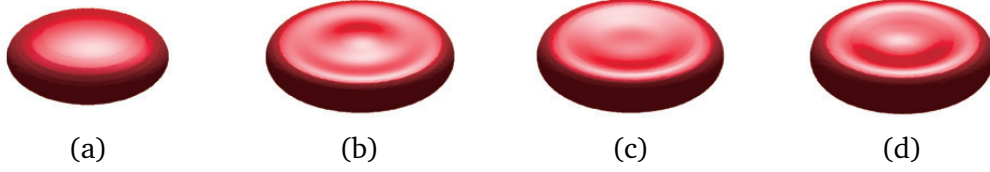
<center>(a)   (b)   (c)   (d)</center>

Figure 11: Temporal evolution of the vesicle membrane in 3D. Reprinted from Shin et al. [39] with permission of Wiley.

2. Various initial conditions

We present various initial conditions in the numerical domain. The various initial conditions to be introduced below are often used in many papers dealing with the phase-field models, which are intended to be expressed using finite difference methods. We first discretize a two-dimensional domain, i.e., $\Omega = (a, b) \times (c, d)$. Let N_x and N_y be positive integers, $h = (b-a)/N_x = (d-c)/N_y$ be the uniform mesh size, $\Omega_h = \{(x_i, y_j) : x_i = a+(i-0.5)h, y_j = c+(j-0.5)h, 1 \leq i \leq N_x, 1 \leq j \leq N_y\}$ be the set of cell-centers, and $t^n = n\Delta t$ be the discrete time. Here, Δt is the time step. Let ϕ_{ij}^n be a numerical approximation of $\phi(x_i, y_j, t^n)$. The three-dimensional (3D) case is a simple extension of 2D case. The phase-field ϕ has values from -0.9 to 0.9 across interfacial transition layer over $2\sqrt{2}\epsilon \tanh^{-1}(0.9)$ length [28]. Hence, if we let $2\sqrt{2}\epsilon \tanh^{-1}(0.9) = hm$, then the interfacial length parameter $\epsilon = \epsilon_m = hm/[2\sqrt{2}\tanh^{-1}(0.9)]$. Here, ϵ_m means that we have nearly mh transition layer width and is used for our all experiments.
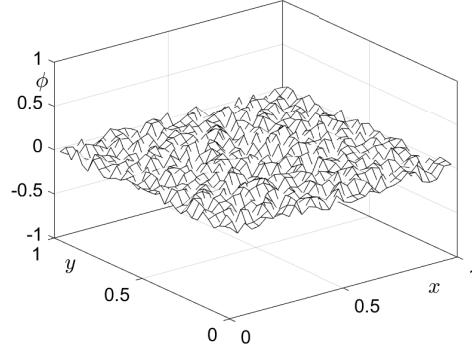
2.1. Random initial condition

The initial state is taken to be $\phi_{ij}^0 = \phi_{ave} + A \, \text{rand}(x, y)$, where ϕ_{ave} is average concentration, A is the amplitude of the perturbation and $\text{rand}(x, y)$ is an uniformly distributed random number between -1 and 1. In other words, random initial condition for the phase-field model is that the initial value of ϕ_{ij}^0 is given in random numbers between -1 and 1. When we use the random initial condition, we can show how well the phase model like the CH equation applies. Figure 12 shows a random initial condition for $\phi_{ave} = 0$ with $A = 0.1$ on the computational domain $\Omega = (0, 1) \times (0, 1)$.

2.2. Initial conditions for a convergence test

To show the temporal accuracy, the authors in [59] considered the following initial condition on $\Omega = (0, 2\pi) \times (0, 2\pi)$ (see Fig. 13(a)):
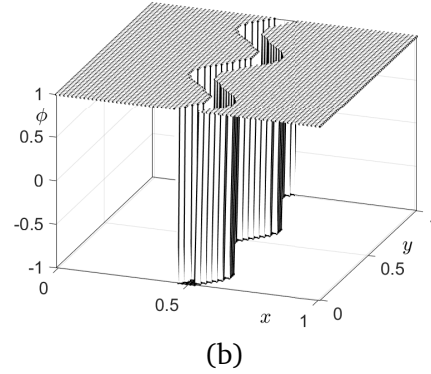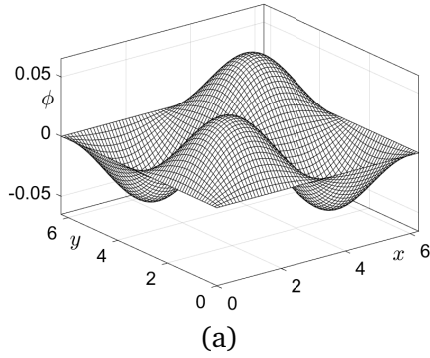
$$\phi(x, y, 0) = 0.05 \sin x \sin y.$$

The authors have obtained the reference numerical solution at a certain time with a 400×400 mesh, the time step $\Delta t = 10^{-4}$, and $\epsilon = 0.1$. In [23], another initial condition was used for a numerical convergence test, see Fig. 13(b). The initial condition

Figure 12: Random initial condition with $\phi_{ave} = 0$ and $A = 0.1$.

$\phi(x, y, 0)$ on $\Omega = (0, 1) \times (0, 1)$ is given as

$$\phi(x, y, 0) = \begin{cases} 1 & \text{if } x > \dfrac{1}{12.8}\sin(4\pi y) + 0.5 + 0.045, \\ 1 & \text{if } x < \dfrac{1}{12.8}\sin(4\pi y) + 0.5 - 0.045, \\ -1 & \text{otherwise.} \end{cases} \tag{2.1}$$

Figure 13: (a) $\phi(x, y, 0) = 0.05 \sin x \sin y$. (b) Mesh plot of the initial condition given by Eq. (2.1).

2.3. Rounded rectangle

In [31], the authors consider a rounded rectangle on the unit domain as an initial condition given by

$$\phi(x, y, 0) = \begin{cases} \tanh\left(\frac{b-y}{\sqrt{2}\epsilon}\right), & \text{for } x \leq a - r, \ y \geq b - r \\ \tanh\left(\frac{a-x}{\sqrt{2}\epsilon}\right), & \text{for } x > a - r, \ y < b - r \\ \tanh\left(\frac{r - \sqrt{(x-a+r))^2 + (y-b+r))^2}}{\sqrt{2}\epsilon}\right), & \text{for } x > a - r, \ y > b - r \\ -1, & \text{otherwise.} \end{cases} \tag{2.2}$$

This initial condition is designed to deal with a 2D dam break problem which is a representative problem of the two-phase flow test problems. The parameters $a = 0.3$, $b = 0.5$, and $r = 0.04$ are the width, height, and the radius of the curve of the rounded rectangle, respectively. Figure 14 shows the initial condition with the uniform mesh size $h = 1/64$ and $\epsilon = \epsilon_2$ on the computational domain $\Omega = (0, 1) \times (0, 1)$.
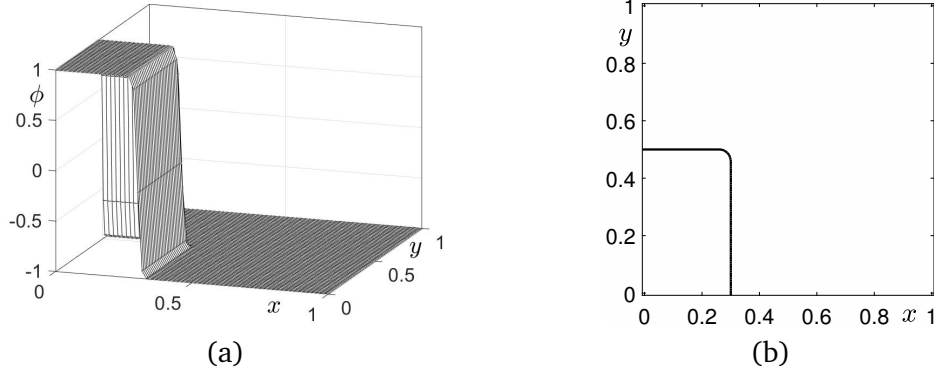

Figure 14: Rectangle with a rounded corner: (a) mesh plot of the phase-field $\phi(x, y, 0)$ and (b) the contour plot of $\phi(x, y, 0)$ at the zero level.

2.4. Initial conditions from a signed distance function

In this section, we consider making initial conditions from a signed distance function.

2.4.1. Circle and ellipse

Let us consider an ellipse.

$$\frac{x^2}{a^2} + \frac{y^2}{b^2} = 1, \tag{2.3}$$

where a and b are the semi-major and semi-minor axes, respectively. When $a = b = r$, Eq. (2.3) becomes a circle with radius r:

$$x^2 + y^2 = r^2.$$

As the initial conditions, the shapes of circle and ellipse have been used for simulation of the CH equation and the AC equation [13, 17, 50, 57]. We set the initial condition of circle in the domain $\Omega = (-1.2, 1.2) \times (-1.2, 1.2)$ as follows.

$$\phi(x, y, 0) = \tanh\left(\frac{r - \sqrt{x^2 + y^2}}{\sqrt{2}\epsilon}\right). \tag{2.4}$$
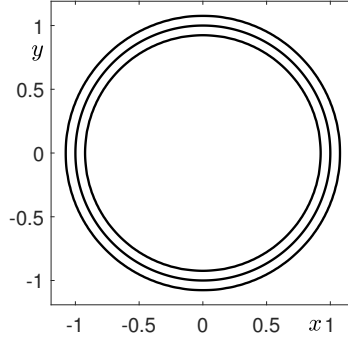
Figure 15: Contour plot of Eq. (2.4) at values $-0.9, 0$, and 0.9.

Figure 15 shows the contour plot of Eq. (2.4) at values $-0.9, 0$ and 0.9. Here, $r = 1$, $h = 2.4/128$, $\epsilon = \epsilon_8$, and a mesh grid 128×128 are used.

To be consistent with Eq. (2.4), for the general elliptical shape, we may consider the following form in the domain $\Omega = (-2.4, 2.4) \times (-2.4, 2.4)$:

$$\phi(x, y, 0) = \tanh\left(\frac{\sqrt{ab} - \sqrt{bx^2/a + ay^2/b}}{\sqrt{2}\epsilon}\right). \tag{2.5}$$

$a = 2$, $b = 0.5$ and mesh grid 256×256 are used and remaining parameters are as described above. Figure 16(a) shows contour of Eq. (2.5) at the levels $\phi = -0.9, 0, 0.9$. From a simple calculation, we can derive the maximum and the minimum of the transition width from $\phi = -0.9$ to $\phi = 0.9$ as $\sqrt{\frac{8a}{b}}\epsilon \tanh^{-1}(0.9)$ and $\sqrt{\frac{8b}{a}}\epsilon \tanh^{-1}(0.9)$, respectively. Figure 16(b) shows the maximum and the minimum of the transition width against a values with $b = 0.5$. Here, we scaled the maximum and the minimum values by the transition width of the circular shape, i.e., $\sqrt{8}\epsilon \tanh^{-1}(0.9)$.

However, this kind of interfacial profile does not match the actual phenomena, especially in fluid dynamics combined with the phase-field model. The reason is that it assumes an equilibrium state in computing variables such as surface tension; it implies that formula have been derived under the assumption such that the interfacial length in local coordinates follows the hyperbolic tangent profile. To confirm this numerically, the circumference of the ellipse is measured using the Dirac-delta function [34] and compared with the reference approximation L, which is based on the series solution, listed as follows:

$$L = \pi(a + b)\left(1 + \frac{3s}{10 + \sqrt{4 - 3s}}\right), \tag{2.6}$$

where $s = (a - b)^2/(a + b)^2$. We choose the Dirac-delta function as $|\nabla\phi|$. Table 1 shows the circumference of ellipse before and after modification.

Now, we suggest how to make an ellipse whose contours are uniform in any direction. First, spread n points on the ellipse. Second, for a fixed point (x_i, y_j), measure the distances with each point on the curve and set the minimum value among the
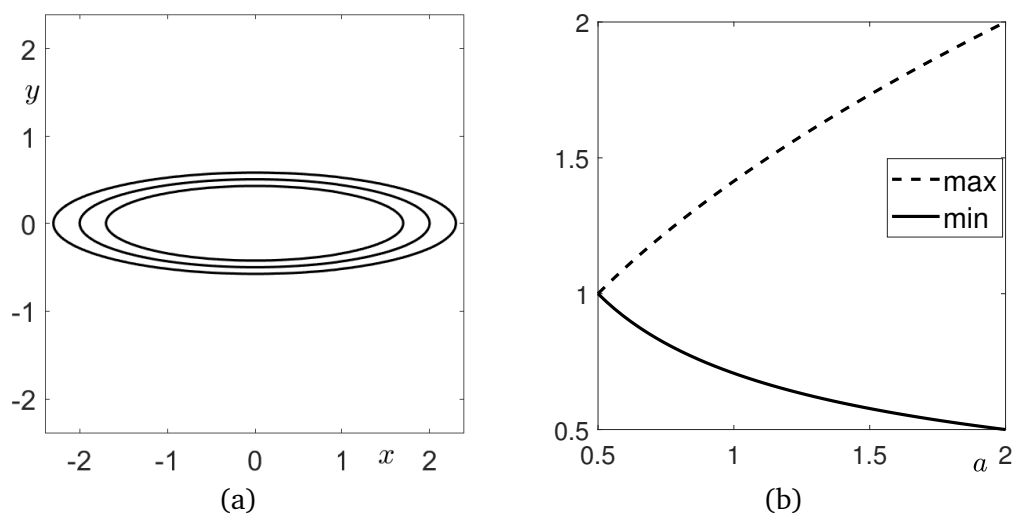
Figure 16: (a) Contour plot of Eq. (2.5) at the levels $\phi = -0.9, 0, 0.9$. (b) The scaled maximum ($\sqrt{a/b}$) and minimum ($\sqrt{b/a}$) of the transition width against a with b.

Table 1: Circumference of ellipse with uniform and non-uniform interfacial thickness.

Types	Uniform	Non-uniform	Reference
Circumference	3.4315	3.4301	3.4314

distances as d_{ij}. Third, if $x_i^2/a^2 + y_j^2/b^2 > 1$ (outside the ellipse), then redefine the distance as $d_{ij} = -d_{ij}$. Repeat these three steps for all i and j, and we finally set $\phi_{ij}^0 = \tanh(d_{ij}/(\sqrt{2}\epsilon))$. See Fig. 17(a) for the schematic illustration of defining distance function and Fig. 17(b) for the result using the proposed algorithm. As shown in Fig. 16(a) and Fig. 17(b), the ellipse used only tanh function has uneven thickness at each level. Conversely, the ellipse applied our proposed method has uniform thickness at each level, regardless of the horizontal or vertical direction.
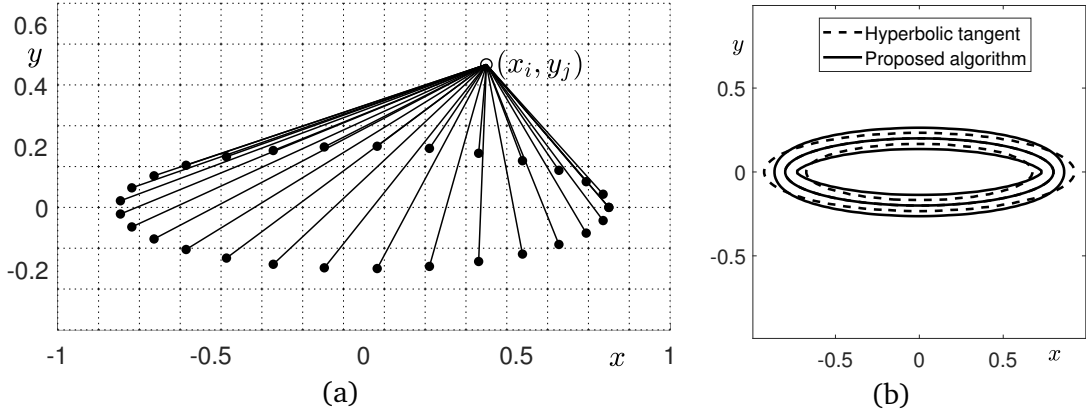

Figure 17: (a) Schematic of defining distance function. (b) An example of contour plot of general ellipse (dashed line) and ellipse obtained from the proposed algorithm (solid line).

2.4.2. Multiple isolated circles with random radius

In two-dimensional space, let us consider the following initial condition composed of k isolated circles. In general,

$$\phi(x, y, 0) = k - 1 + \sum_{i=1}^{k} \tanh\left(\frac{r_i - \sqrt{(x - x_i)^2 + (y - y_i)^2}}{\sqrt{2}\epsilon}\right), \qquad (2.7)$$

where (x_i, y_i) and $r_i = 0.2$ rand are the center of the i-th circle and its random radius, rand is a uniformly distributed random number between 0 and 1. In Fig. 18, we set 10 isolated circles with arbitrary radius on $\Omega = (-1, 1) \times (-1, 1)$. Here, uniform mesh size $h = 1/64$ and $\epsilon = \epsilon_2$ are used. We can see the mesh plot of the phase-field $\phi(x, y, 0)$ which has the values between -1 and 1 as shown in Fig. 18(a). Furthermore, we can observe the zero-level contour of $\phi(x, y, 0)$ in Fig. 18(b).

2.4.3. Sinusoidal profile

For the initial condition of the RT instability problems [35], sinusoidal profiles are used. Because the RT instability usually requires only a very small perturbation, i.e., a small
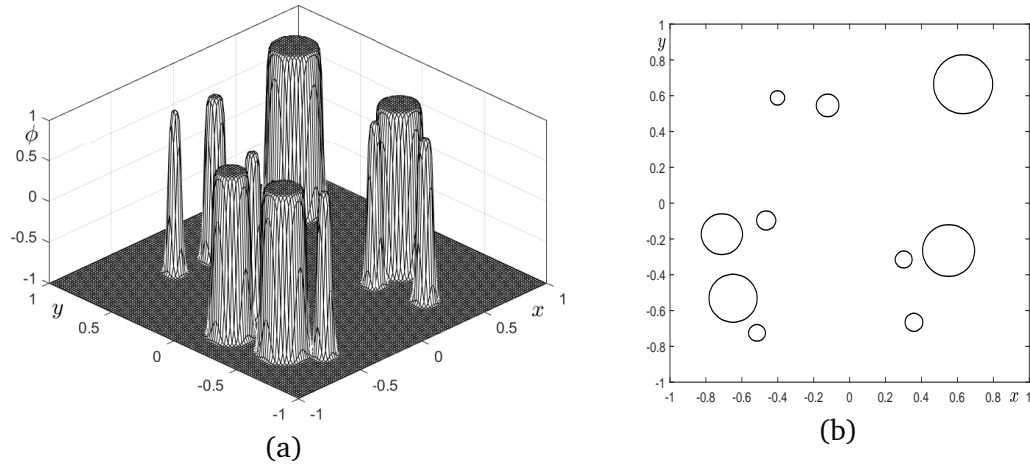
Figure 18: Multiple isolated circles with random radius in the two-dimensional space: (a) mesh plot of the phase-field $\phi(x, y, 0)$ and (b) its zero-level contour.

amplitude, an initial condition can be set by the following equation, for example,

$$\phi(x, y, 0) = \tanh\left(\frac{y - 0.01\cos(2\pi x)}{\sqrt{2}\epsilon}\right), \tag{2.8}$$

where ϵ is a width of interface and $\epsilon = \epsilon_8$ is used. However, if we want a large perturbation and have an uniform thickness at each level, then Eq. (2.8) is not good for an initial condition profile. Contour lines of Eq. (2.8) is not uniform; however, if we apply the method used in ellipse shape, then we have uniform contour lines as shown in Figure 19.
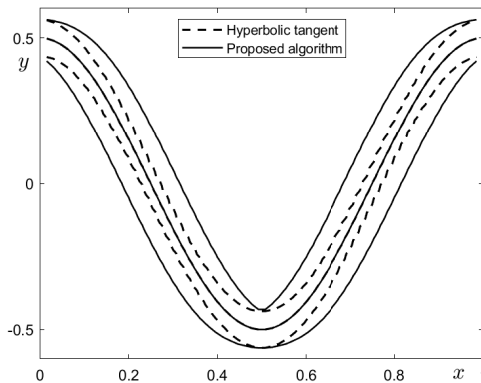

Figure 19: Contour lines at $\phi = -0.9,\ 0,\ 0.9$ using Eq. (2.8) (dashed line) and the proposed algorithm (solid line).

2.4.4. Sphere and ellipsoid

In this section, we consider the initial conditions for a sphere [20] and an ellipsoid [19]. The initial condition of sphere is defined on $\Omega = (-1.2, 1.2)^3$ as follows:

$$\phi(x, y, z, 0) = \tanh\left(\frac{r - \sqrt{x^2 + y^2 + z^2}}{\sqrt{2}\epsilon}\right). \tag{2.9}$$

Figure 20(a) shows the initial phase condition of sphere at the levels at -0.9, 0, and 0.9. Here, $r = 1$, $h = 2.4/128$, $\epsilon = \epsilon_8$, and a mesh grid $N_x \times N_y \times N_z = 128 \times 128 \times 128$ are used.
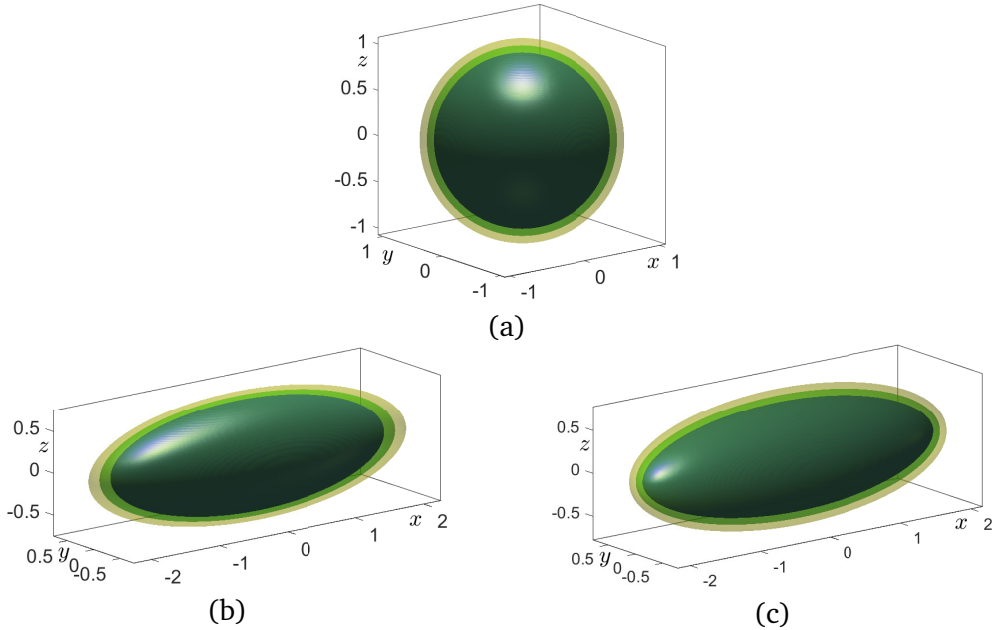

(a)

(b)   (c)

Figure 20: (a) Isosurface of Eq. (2.9)) at the levels $\phi = -0.9$, 0, and 0.9. (b) Isosurface of Eq. (2.10) at the levels $\phi = -0.9$, 0, and 0.9. (c) Isosurface of proposed algorithm at the levels $\phi = -0.9$, 0, and 0.9.

To be consistent with Eq. (2.9), for the ellipsoid, we consider the following form in 3D space $\Omega = (-2.4, 2.4) \times (-1.2, 1.2) \times (-1.2, 1.2)$:

$$\phi(x, y, z, 0) = \tanh\left(\frac{\sqrt[3]{abc} - \sqrt[3]{abc}\sqrt{x^2/a^2 + y^2/b^2 + z^2/c^2}}{\sqrt{2}\epsilon}\right). \tag{2.10}$$

Figure 20(b) shows the isosurfaces of the ellipsoidal initial condition at the levels at $\phi = -0.9$, 0 and 0.9 with $a = 2.1$, $b = c = 0.7$, $\epsilon = \epsilon_8$, and a mesh grid $N_x \times N_y \times N_z = 256 \times 128 \times 128$.

Now, we also make an ellipsoid whose isosurfaces are uniform in any direction. First, spread n points on the ellipsoid. Second, for a fixed point (x_i, y_j, z_k), measure the distances with each point on the surface and put the minimum value among the

distances as d_{ijk}. Third, if $x_i^2/a^2 + y_j^2/b^2 + z_k^2/c^2 > 1$ (outside the ellipsoid), then redefine it value as $d_{ijk} = -d_{ijk}$. Repeating these three steps for all i, j, and k, and we finally set $\phi_{ijk} = \tanh(d_{ijk}/(\sqrt{2}\epsilon))$. Figure 20(c) shows the initial condition of ellipsoid at the levels $\phi = -0.9$, 0, and 0.9 by using the proposed algorithm. Like the above case of ellipse, the thickness between levels in any directions is not even. However, the ellipsoid obtained by our algorithm has uniform isosurfaces in any direction.

2.4.5. Torus

Next, we consider a torus, which is a surface of revolution generated by revolving a circle in 3D space about an axis. The radius of big circle is known as the major radius R and small one is the minor radius r. In [19], the authors presented not only ellipsoid but also torus as initial condition. There exist two kinds of torus: symmetric and non-symmetric. An initial condition for the torus at the center $(0, 0, 0)$ and on $\Omega = (-1.5, 1.5) \times (-1.5, 1.5) \times (-0.75, 0.75)$ is given as

$$\phi(x, y, z, 0) = \tanh\left(\frac{r^2 - \left(R - \sqrt{x^2 + y^2}\right)^2 - z^2}{\sqrt{2}\epsilon}\right). \tag{2.11}$$

Figure 21(a) shows the isosurface of ϕ at the levels -0.9, 0, 0.9 for the radially symmetric torus with $R = 0.6$ and $r = 0.3$ about the z-axis. Figure 21(b) and (c) show the isosurfaces of ϕ at the levels -0.9, 0, 0.9 for the radially non-symmetric torus with $R = 0.6$, and $r = 0.05\sin(\arctan(y, x)) + 0.3$ about the z-axis, Eq. (2.11) and the proposed algorithm, respectively. Here, $h = 3/128$, $\epsilon = \epsilon_4$, and a mesh grid $N_x \times N_y \times N_z = 128 \times 128 \times 64$.

2.4.6. Triply periodic minimal surfaces

For the next step, there are widely used stuff in biotechnology named triply periodic minimal surfaces, which are approximated by periodic nodal surfaces approximation [25]. The followings are periodic nodal surfaces approximations of triply periodic minimal surfaces, named Schwarz primitive (P), Schwarz diamond (D), and Gyroid (G), respectively.

$$\cos(2\pi x) + \cos(2\pi y) + \cos(2\pi z) = 0, \tag{2.12}$$

$$\cos(2\pi x)\cos(2\pi y)\cos(2\pi z) - \sin(2\pi x)\sin(2\pi y)\sin(2\pi z) = 0, \tag{2.13}$$

$$\sin(2\pi x)\cos(2\pi y) + \sin(2\pi z)\cos(2\pi x) + \sin(2\pi y)\cos(2\pi z) = 0, \tag{2.14}$$

where $x, y, z \in [0, 1]$. Since these periodic representations are not matched to the Euclidean distance, these cause the problems that one might perform a further process to establish an equilibrium profile. One of the possible solutions is to use cut-off and relaxation [54]. Figure 22(a)–(c) show the periodic nodal surfaces approximations of P, D, and G surfaces, respectively, and Fig. 22(d)–(f) show the reconstructed approximations of P, D, and G surfaces, respectively, followed by Step 1 to 6 in [54].
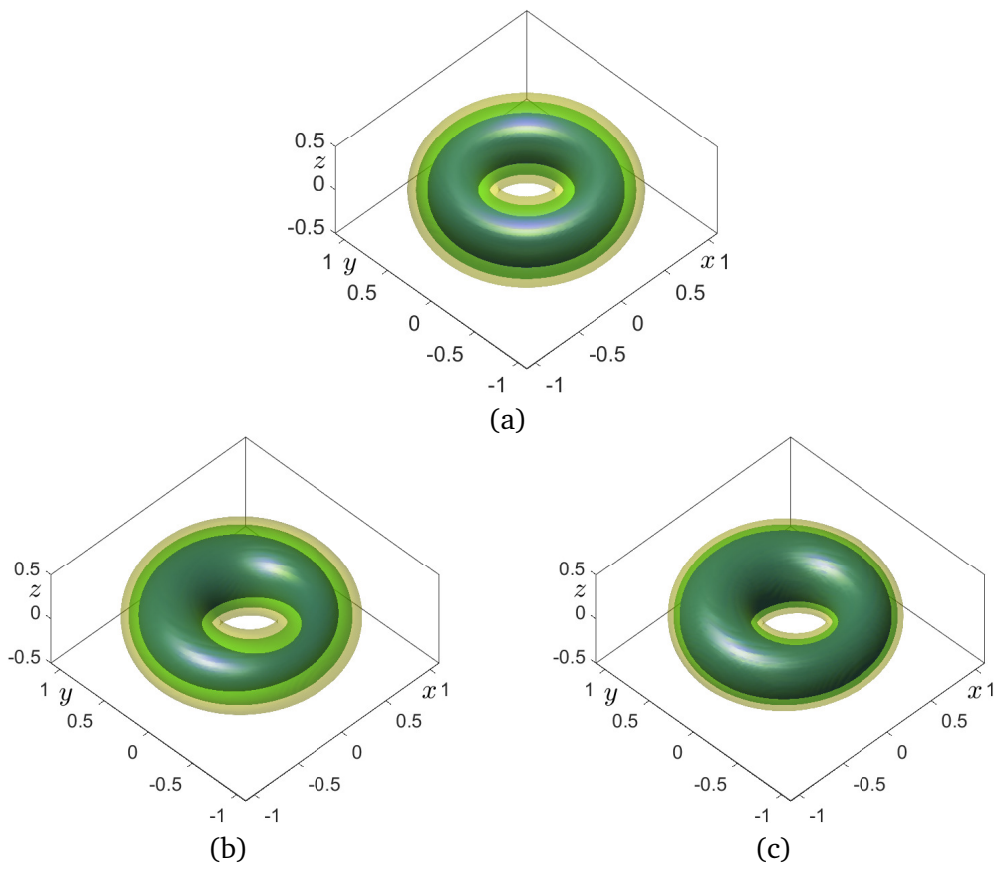
Figure 21: (a) is radially symmetric torus. (b) and (c) are radially non-symmetric tori about the z-axis with Eq. (2.11) and the proposed algorithm, respectively.
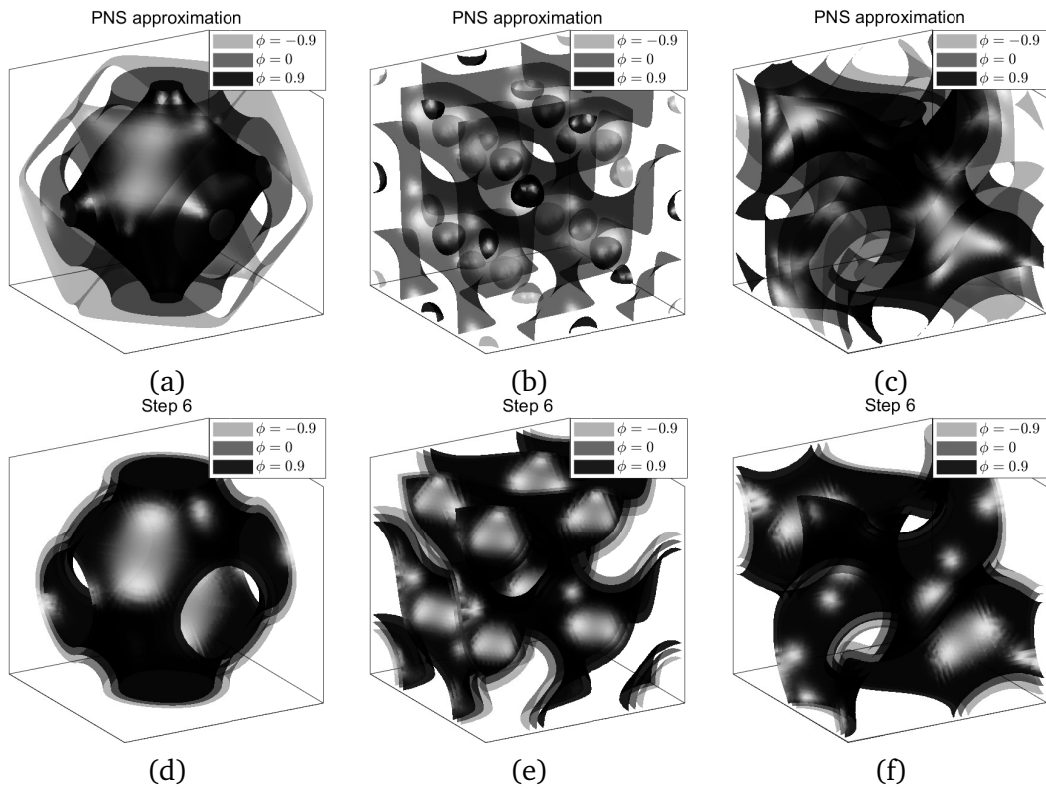
Figure 22: (a)–(c) are the periodic nodal surfaces approximations of P, D, and G surfaces, respectively, which are represented by Eqs. (2.12)–(2.14). (d)–(f) are reconstructed profile of P, D, and G surfaces which can be employed to the initial conditions for the phase-field models. The process is followed by Step 1 to 6 in [54].

2.5. Periodic waves on curve and surface

Initially periodic waves on closed curves or surfaces are often provided to investigate the property of mean curvature flow, a dendrite pattern formation, etc [36]. To achieve this perturbation in inceptive period, one can use polar and spherical harmonics [16]. The polar harmonics in real parts, or k-fold symmetries are given as

$$W_k(\theta) = \cos\left(k(\theta - \theta_{ref})\right),$$

where k depicts the number of symmetric tips, $\theta = \arctan(y/x) + \pi I(x < 0)$, and θ_{ref} is a given angle. Note that $I(\cdot)$ is an indicator function. Figure 23 depicts the initial states including periodic waves on curves. We use the following equation

$$\phi(x, y, 0) = \tanh\left(\frac{r + AW_k - \sqrt{x^2 + y^2}}{\sqrt{2}\epsilon}\right),$$

where $(x, y) \in [-0.9, 0.9]^2$. Note that r implies radius of circle, A indicates an amplitude of waves. Consequently, the spherical harmonics in real parts are given as
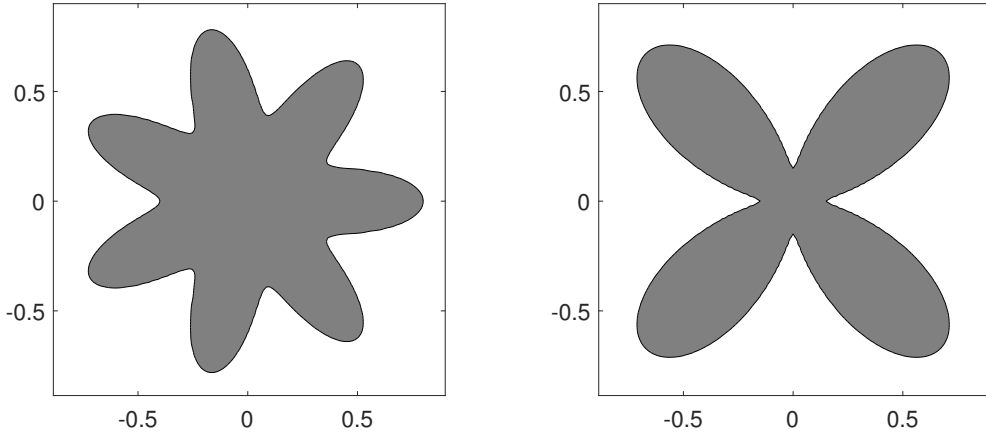
(a) $r = 0.6$, $A = 0.2$, $k = 7$, $\theta_{ref} = 0$.   (b) $r = 0.55$, $A = 0.4$, $k = 4$, $\theta_{ref} = \pi/4$.

Figure 23: Polar harmonics on curves.

$$Y_l^m(\theta, \phi) = \sqrt{\frac{(2l+1)(l-m)!}{4\pi(l+m)!}} P_l^m(\cos\theta) \sin(m\phi),$$

where l is the degree of waves in latitudinal coordinate with $\theta = \arctan(y/x)I(y > 0) + \pi I(x < 0)$, i.e., $\theta \in [0, \pi]$, and m is the order of waves in longitudinal coordinate with $\phi = \text{sgn}(y)\arccos(z/\sqrt{x^2 + y^2 + z^2}) + \pi$, i.e., $\phi \in [0, 2\pi)$. Note that $P_l^m(\cdot)$ is an associated Legendre polynomial. Figure 24 shows the initial states including periodic waves on surfaces. We employ the following equation

$$\phi(x, y, z, 0) = \tanh\left(\frac{r + AY_l^m - \sqrt{x^2 + y^2 + z^2}}{\sqrt{2}\epsilon}\right),$$
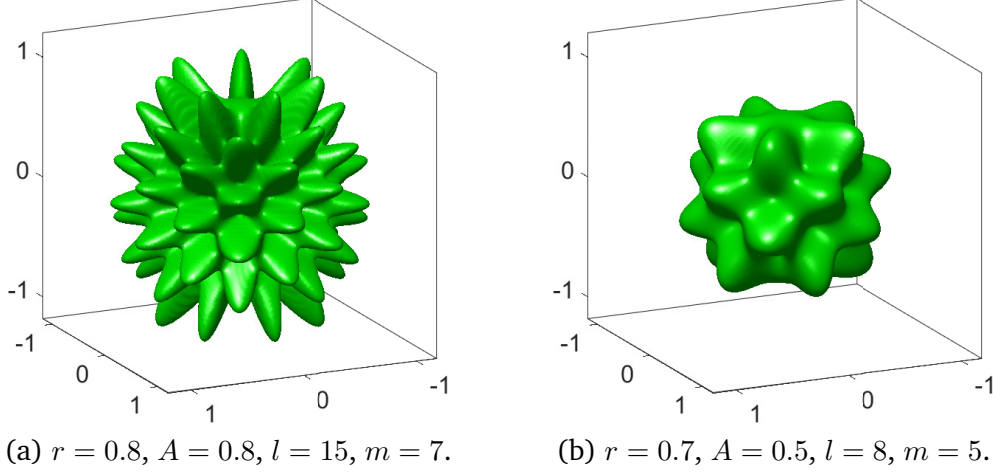
where $(x, y, z) \in [-1.2, 1.2]^3$.

(a) $r = 0.8$, $A = 0.8$, $l = 15$, $m = 7$.   (b) $r = 0.7$, $A = 0.5$, $l = 8$, $m = 5$.

Figure 24: Spherical harmonics on spheres.

2.6. Initial conditions with the same total concentration

Let us consider making initial conditions of a circle and an ellipse which have the same area. For example, if the circle's radius is r and the ellipse's major and minor axes are a and b, then the areas are πr^2 and πab, respectively. As a concrete example, we consider $r = 1$, $a = 2$, and $b = 0.5$. Under these settings, the analytic area is the same as π. However, because we deal with numerical solution, the numerical areas are different. We set two conditions using $\tanh$ function in $(-2.4, 2.4) \times (-2.4, 2.4)$ with a mesh grid 128×128. One is the ϕ_{ij}^c meaning a circle with $r = 1$ at zero level, and the other is ϕ_{ij}^e that means an ellipse with $a = 2$ and $b = 0.5$ at zero level.

$$\phi_{ij}^c = \tanh\left(\frac{1 - \sqrt{x^2 + y^2}}{\sqrt{2}\epsilon}\right),$$

$$\phi_{ij}^e = \tanh\left(\frac{1 - \sqrt{x^2/4 + 4y^2}}{\sqrt{2}\epsilon}\right).$$

Fig. 25(a) and (b) show mesh plot of ϕ_{ij}^c with $r = 1$ and ϕ_{ij}^e with $a = 2$ and $b = 0.5$, respectively.

In general, the total concentrations of ϕ_{ij}^c and ϕ_{ij}^e are different, i.e.,

$$\sum_{i=1}^{N_x}\sum_{j=1}^{N_y}\phi_{ij}^c \neq \sum_{i=1}^{N_x}\sum_{j=1}^{N_y}\phi_{ij}^e.$$
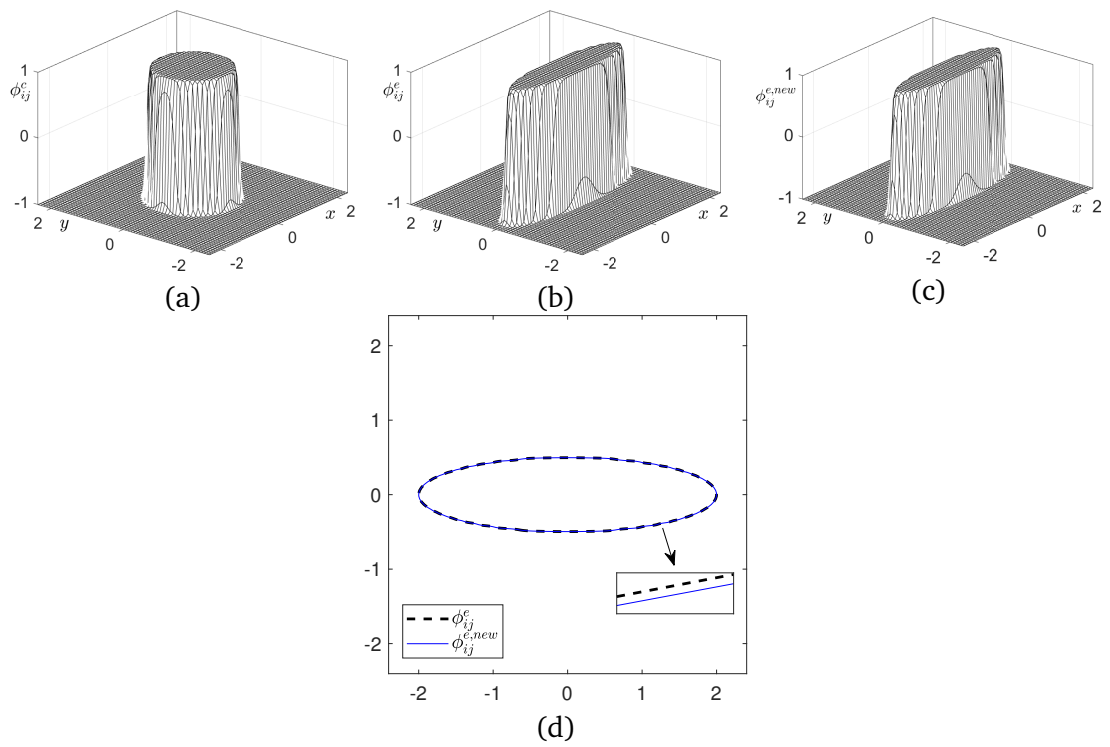
Figure 25: (a) Mesh of ϕ_{ij}^c. (b) Mesh of ϕ_{ij}^e. (c) Total concentration corrected ellipse, $\phi_{ij}^{e,new}$. (d) Contours of ϕ_{ij}^e and $\phi_{ij}^{e,new}$ at zero-level.

We use the following correction to make the total concentration of the ellipse the same as that of the circle.

$$\phi_{ij}^{e,new} = \phi_{ij}^e + \alpha F(\phi_{ij}^e),$$

where α is a constant and $F(\phi) = 0.25(\phi^2 - 1)^2$. $F(\phi) = 0.25(\phi^2 - 1)^2$ is known as a double well potential energy. To find the value of α, we set

$$\sum_{i=1}^{N_x} \sum_{j=1}^{N_y} \phi_{ij}^c = \sum_{i=1}^{N_x} \sum_{j=1}^{N_y} \phi_{ij}^{e,new} = \sum_{i=1}^{N_x} \sum_{j=1}^{N_y} [\phi_{ij}^e + \alpha F(\phi_{ij}^e)].$$

Then, α is given as

$$\alpha = \frac{\sum_{i=1}^{N_x} \sum_{j=1}^{N_y} (\phi_{ij}^c - \phi_{ij}^e)}{\sum_{i=1}^{N_x} \sum_{j=1}^{N_y} F(\phi_{ij}^e)}.$$

Using this α, we can derive new total concentration $\phi_{ij}^{e,new}$ which is more similar with ϕ_{ij}^c. This algorithm has the advantage of being able to reduce error without losing concentrations. Figure 25(c) shows the mesh plot of $\phi_{ij}^{e,new}$ which is similar to ϕ_{ij}^e. However, as shown in Fig. 25(d), two contours of ϕ_{ij}^e and $\phi_{ij}^{e,new}$ at zero-level differ when they are viewed closely. In fact, we got the numerical area of circle and ellipse as 3.1398 and 3.1384, respectively. The numerical area of the corrected ellipse is 3.1394, which is close to the area of circle.

2.7. Initial condition from an image

In this section, we consider making an initial condition from an image by using an image segmentation process [29]. The image segmentation method is based on the following equation:

$$\frac{\partial \phi(\mathbf{x}, t)}{\partial t} = g(f_0(\mathbf{x})) \left(-\frac{F'(\phi)}{\epsilon^2} + \Delta\phi \right) + \lambda g(f_0(\mathbf{x})) F(\phi).$$

Here, $f_0(\mathbf{x}) = (f(\mathbf{x}) - f_{\min})/(f_{\max} - f_{\min})$, where $f_{\max}$ and $f_{\min}$ are the maximum and minimum values of the given image $f(\mathbf{x})$, respectively. $g(f_0(\mathbf{x}))$ is the edge stopping function which acts to stop the evolution when the contour reaches the edge. In Fig. 26, we use $\lambda = 10^{-4}$, $\epsilon = \epsilon_4$, $h = 1/64$, $\Delta t = 10^{-5}$, and 64×64 mesh grid. We set $\phi(\mathbf{x}, 0)$ as $\phi(\mathbf{x}, 0) = -1$ if $\mathbf{x}$ is inside two square contour (green line) and $\phi(\mathbf{x}, 0) = 1$ otherwise (see the first column in Fig. 26). The initial data evolves until it reaches the boundary of the image through the motion by mean curvature and the term $\lambda g(f_0(\mathbf{x})) F(\phi)$.
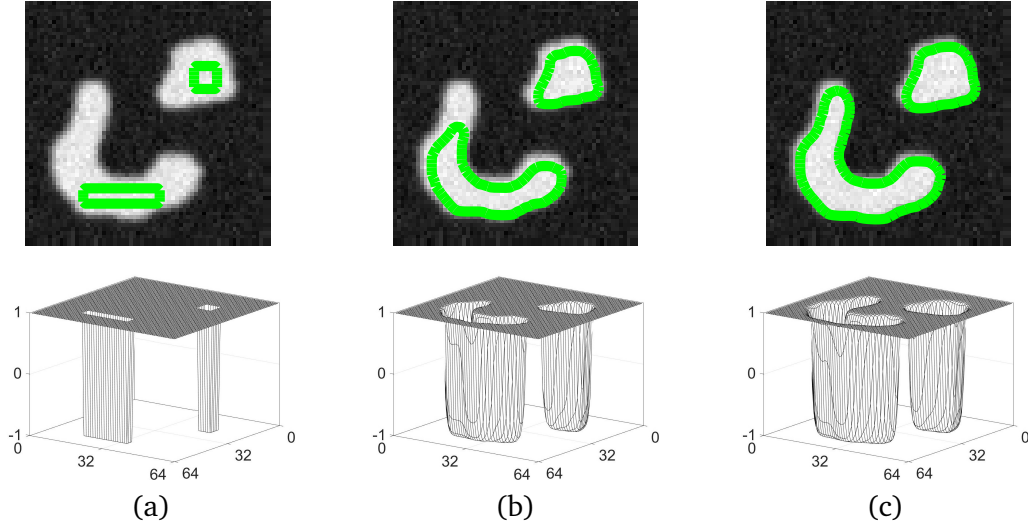
Figure 26: Image segmentation process at (a) 0 iteration, (b) 300 iterations, and (c) 1200 iterations.

2.8. Random initial conditions for multi-component mixture

In this part, we consider two random initial conditions for the multi-component CH equation, the multi-component CH equation can be written as

$$\frac{\partial c_i}{\partial t} = \nabla \cdot (M(\mathbf{c})\nabla\mu_i),$$
$$\mu_i = F'(c_i) - \epsilon^2\Delta c_i + \beta(\mathbf{c}),$$

where c_i and μ_i represent the specific mole fraction and chemical potential for $i = 1, 2, ..., N$, $F(c_i) = 0.25c_i^2(1-c_i)^2$. Let $M(\mathbf{c}) = M = 1$ be a constant mobility. $\beta(\mathbf{c}) = \frac{1}{N}\sum_{i=1}^{N} F'(c_i)$ is a Lagrange multiplier which maintains the summation of total mole fractions be 1 (i.e., $c_1 + c_2 + ... + c_N = 1$) [4]. In the numerical tests, we use $N = 5$ on $\Omega = (0, 1) \times (0, 1)$, the other numerical parameters are $h = 1/128$, $\Delta t = 0.2h$, and $\epsilon = 0.0047$. The first initial condition is

$$c_1(x, y, 0) = 0.2 + 0.01\text{rand}, \ c_2(x, y, 0) = 0.2 + 0.01\text{rand},$$
$$c_3(x, y, 0) = 0.2 + 0.01\text{rand}, \ c_4(x, y, 0) = 0.2 + 0.01\text{rand},$$
$$c_5(x, y, 0) = 1 - c_1(x, y, 0) - c_2(x, y, 0) - c_3(x, y, 0) - c_4(x, y, 0),$$

where rand represents a random number between -1 and 1. The second one is

$$c_1(x, y, 0) = 1, c_2(x, y, 0) = ... = c_5(x, y, 0) = 0 \quad \text{if rand}' < \frac{1}{5},$$

$$c_2(x, y, 0) = 1, c_1(x, y, 0) = ... = c_5(x, y, 0) = 0 \quad \text{else if rand}' < \frac{2}{5},$$

$$c_3(x, y, 0) = 1, c_1(x, y, 0) = ... = c_5(x, y, 0) = 0 \quad \text{else if rand}' < \frac{3}{5},$$

$$c_4(x, y, 0) = 1, c_1(x, y, 0) = ... = c_5(x, y, 0) = 0 \quad \text{else if rand}' < \frac{4}{5},$$

$$c_5(x, y, 0) = 1, c_1(x, y, 0) = ... = c_4(x, y, 0) = 0 \quad \text{otherwise},$$

where rand$'$ represents the random number between 0 and 1. For convenience, the Case 1 and Case 2 are used to indicate the first and second initial conditions, respectively. Figure 27(a) and (c) show the initial condition of c_1 for Case 1 and Case 2, (b) and (d) are the corresponding evolutional results of c_1 at $t = 1.4063$. We can observe that the initial perturbation of Case 1 becomes flat with time proceeds. On the contrary, the phase separation evolves for Case 2. Therefore, if we want to simulate the multi-component phase separation with randomly distributed initial conditions, the Case 2 is a good choice.
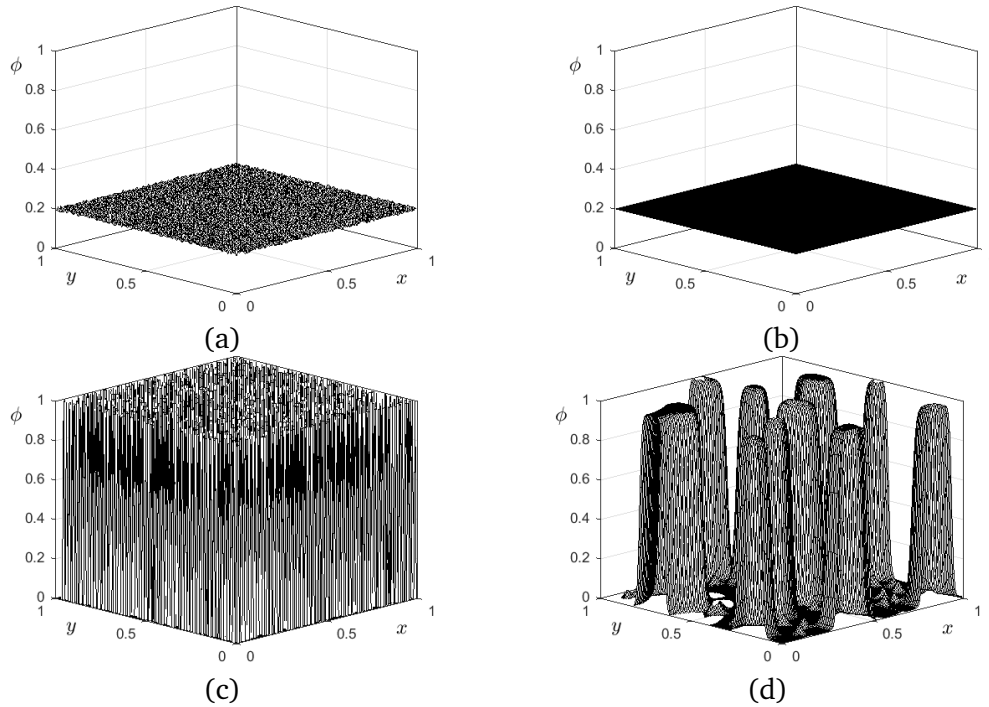

Figure 27: Temporal evolutions with two different initial conditions. (a) and (c) are the initial conditions of c_1 for Case 1 and Case 2. (b) and (d) are the corresponding evolutional results of c_1 at $t = 1.4063$.

2.9. Initial condition using Voronoi diagram

The Voronoi diagram partitions the given domain with seed points onto disjoint polygons. There is one polygon consisting of all points closer to that seed point than any other points for each seed point. Figure 28 shows that the result of evolution with a certain initial condition [51]. This suggests that it may be more efficient and

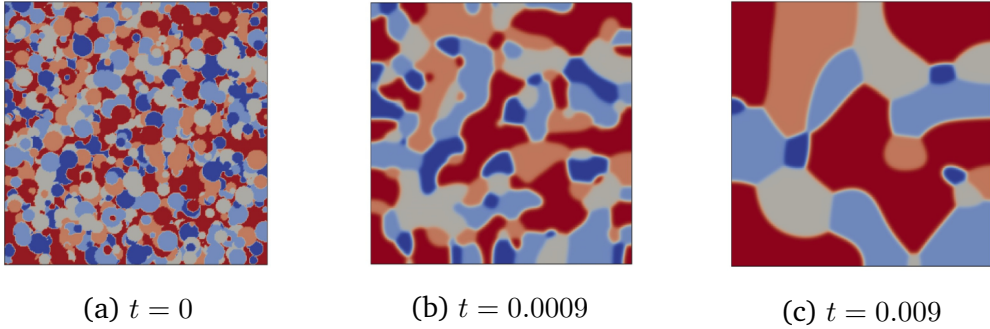(a) $t = 0$ (b) $t = 0.0009$ (c) $t = 0.009$

Figure 28: Result of evolution to morphologies during a spinodal phase separation of 5-component system with average composition. Reprinted from [51] with permission of Elsevier Science. For interpretation of the colors in the figures, the reader is referred to the web version of this article.

natural when the Voronoi diagram is used as an initial condition to obtain the local equilibrium solution in multi-component phase-field models since the final shape of separation is the union of Voronoi polygons. Let us consider N-component phase-field system, i.e., $c_1, c_2, \ldots, c_N$. Let (X_l, Y_l), $l = 1, \ldots, M$ be the seed points. For all $l = 1, \ldots, M$, we assign one to a randomly chosen concentration field and zero to the other concentration fields for the polygon including a seeding point. For example, let $M = 4$, then for some grid point (x_i, y_j) we compute the distances d_l between the grid point and the seed points, (X_l, Y_l), for $l = 1, 2, 3, 4$. Find the index l which makes the minimum distance and assign one to the index l-associated concentration field and zero to the other concentration fields, see Fig. 29(a). We loop over all grid points to define values of the phase-fields. Figure 29(b) and (c) show 30 seed points and the resulting Voronoi diagram using the above procedure.

Figure 30(a)–(d) show mesh plots with four phase-fields for a simplicity.

Three-dimensional Voronoi tessellations have been applied for grain growth simulation. We can straightforwardly extend 2D procedure to 3D procedure for generating 3D Voronoi diagram. Figure 31(a), (b), and (c) show schematic illustration of assigning a concentration value to a grid point, 30 random seed points, and its resulting Voronoi diagram.

Figure 32(a), (b), (c), and (d) show isosurfaces at the $1/2$ level for four concentrations c_1, c_2, c_3, and c_4, respectively.
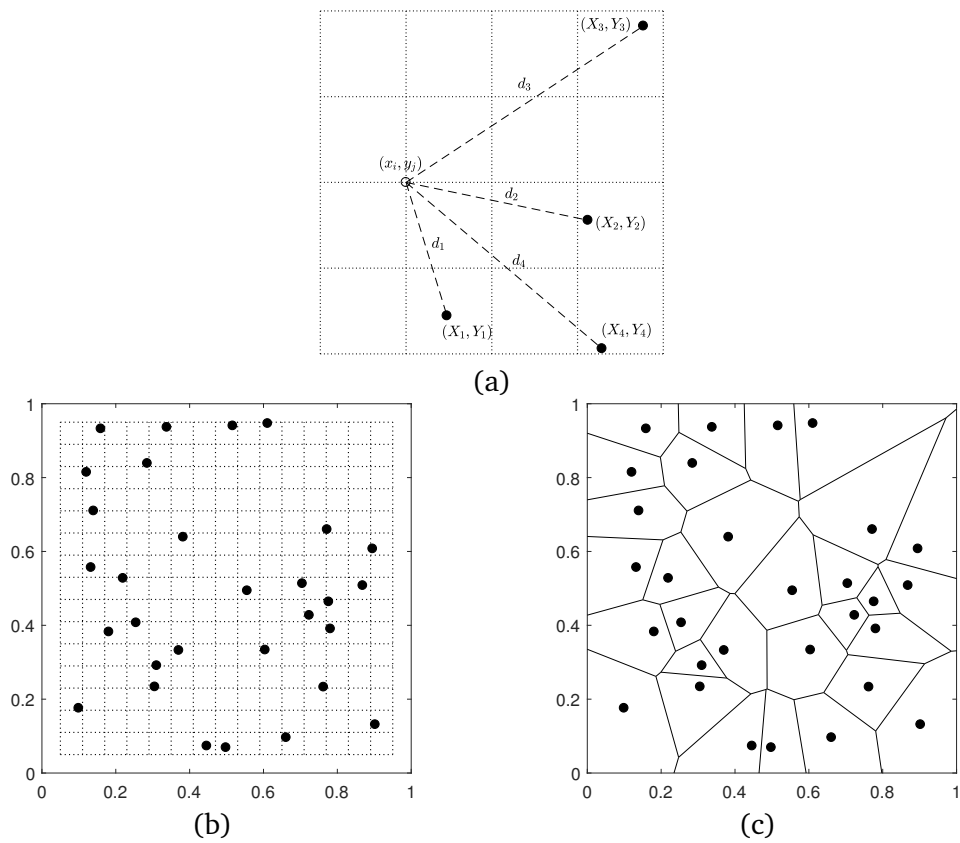
(a)

(b)

(c)

Figure 29: (a) Schematic illustration of assigning a concentration value to a grid point in 2D. (b) 30 seed points. (c) Voronoi diagram.
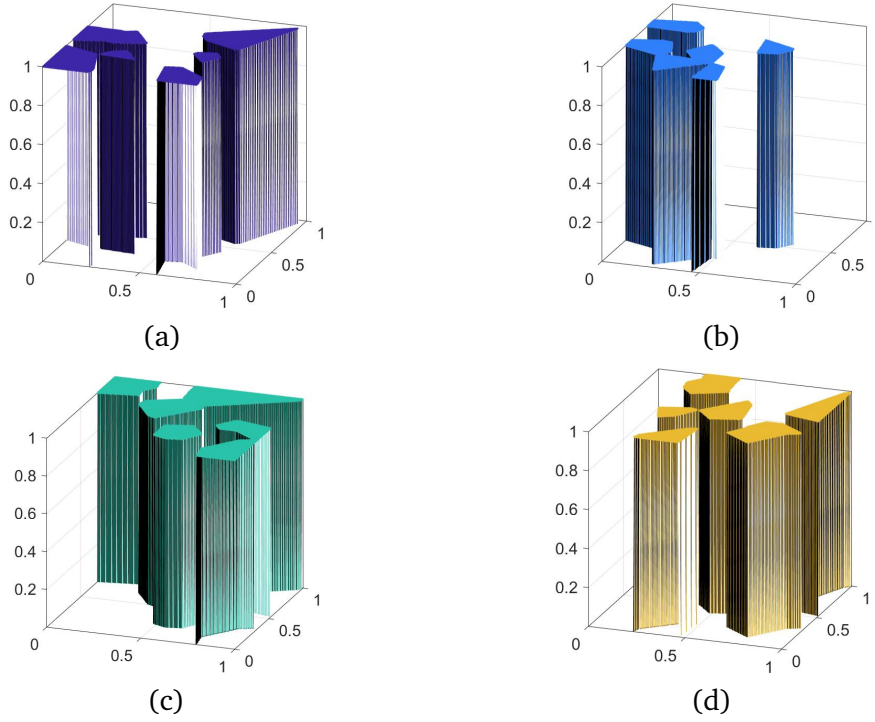
Figure 30: (a), (b), (c), and (d) are mesh plots for concentrations c_1, c_2, c_3, and c_4, respectively.

3. Conclusions

In this paper, we present the necessity of constructing proper initial conditions for the phase-field models. In order to calculate interfacial dynamics numerically and physically correctly, it is important to choose the adequate initial guess. Therefore, we adopt the method of constructing the initial conditions for the simulation suitable for the characteristics of each phase-field model and the effects accordingly. In particular, defining a level set using a signed distance field is essential when investigating phase-field models on a curved surface. If various basic physics laws have to be satisfied, such as preserving mass, decreasing energy, then the constraints can be employed by reflecting the initial conditions.

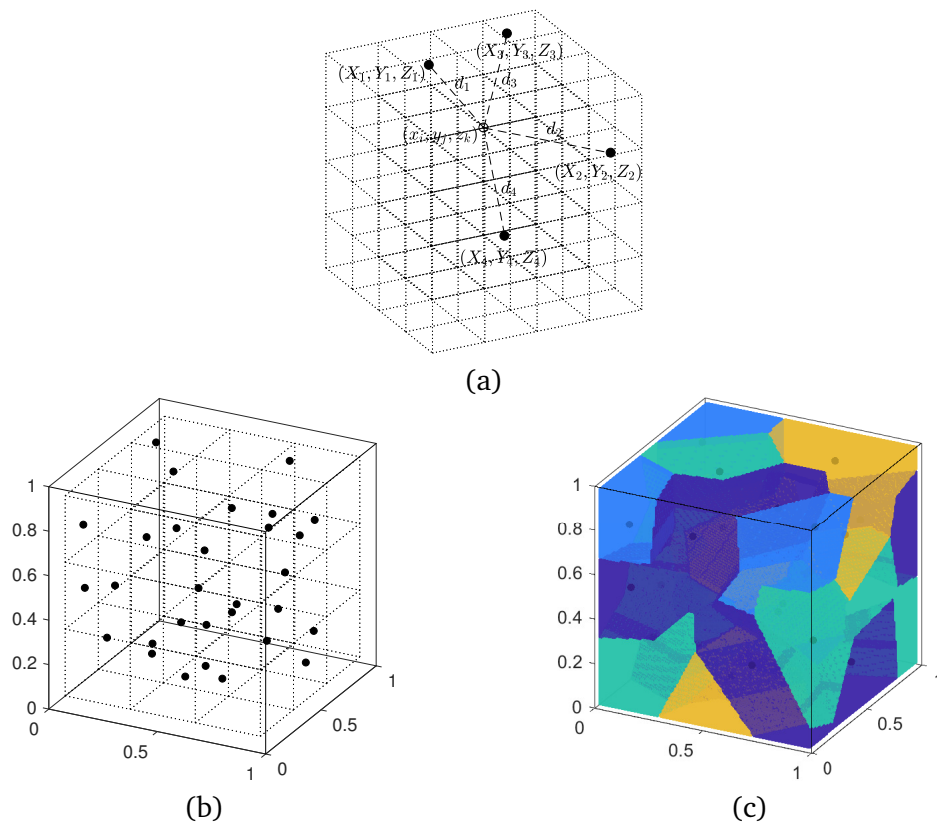## Acknowledgment

(a)

(b)

(c)

Figure 31: (a) Schematic illustration of assigning a concentration value to a grid point in 3D. (b) 30 random seed points in 3D space. (c) Resulting 3D Voronoi diagram.
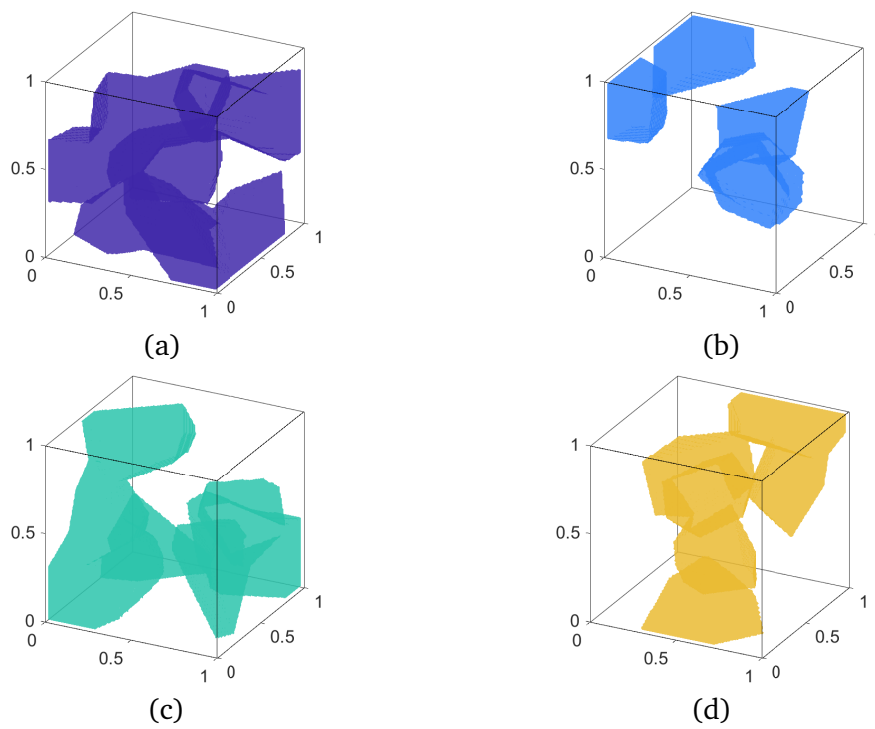
Figure 32: (a), (b), (c), and (d) are isosurfaces at the $1/2$ level for concentrations c_1, c_2, c_3, and c_4, respectively.

References

[1] E. Ahmed, J. Jaffré and J. E. Roberts, *A reduced fracture model for two-phase flow with different rock types*, Math. Comput. Simul. **137**, 49–70 (2017).

[2] S. M. Allen and J. W. Cahn, *A microscopic theory for antiphase boundary motion and itst application to antiphase domain coarsening*, Acta Mater. **27**, 1085–1095 (1979).

[3] F. O. Alpak, B. Riviere and F. Frank, *A phase-field method for the direct simulation of two-phase flows in pore-scale media using a non-equilibrium wetting boundary condition*, Comput. Geosci. **20**, 881–908 (2016).

[4] J. Bosch and M. Stoll, *Preconditioning for vector-valued Cahn–Hilliard equations*, SIAM J. Sci. Comput. **37**, S216–S243 (2015).

[5] A. L. Brkić and A. Novak, *A nonlocal image inpainting problem using the linear Allen–Cahn equation*, In Conference on Non-integer Order Calculus and Its Applications, pp. 229–239. Springer (2018).

[6] T. A. Bubba, D. Labate, G. Zanghirati and S. Bonettini, *Shearlet-based regularized reconstruction in region-of-interest computed tomography*, Math. Model. Nat. Pheno. **13**, 34 (2018).

[7] J. W. Cahn, *On spinodal decomposition*, Acta Mater. **9**, 795–801 (1961).

[8] J. W. Cahn and J. E. Hilliard, *Spinodal decomposition: A reprise*, Acta Mater. **19**, 151–161 (1971).

[9] K. F. Casey, *Periodic traveling-wave solutions to the Whitham equation*, Math. Model. Nat. Pheno. **13**, 16 (2018).

[10] J.M. Church, Z. Guo, P.K. Jimack, A. Madzvamuse, K. Promislow, B. Wetton, S.M. Wise, F. Yang, *High accuracy benchmark problems for Allen–Cahn and Cahn–Hilliard dynamics*, Commun. Comput. Phys. **26**, 947–972 (2019).

[11] J. Shen, X. Yang, *Numerical approximations of Allen–Cahn and Cahn–Hilliard equations*, Discrete Contin. Dyn. Syst. **28**, 1669–1691 (2010).

[12] F. Liu, J. Shen, *Stabilized semi-implicit spectral deferred correction methods for Allen–Cahn and Cahn–Hilliard equations*, Math. Methods Appl. Sci. **38**, 4564–4575 (2015).

[13] Z. Chai, D. Sun, H. Wang and B. Shi, *A comparative study of local and nonlocal Allen–Cahn equations with mass conservation*, Int. J. Heat Mass Transf. **122**, 631–642 (2018).

[14] Q. Cheng, X. Yang and J. Shen, *Efficient and accurate numerical schemes for a hydrodynamically coupled phase field diblock copolymer model*, J. Comput. Phys. **341**, 44–60 (2017).

[15] P. Colli, G. Gilardi and J. Sprekels, *A distributed control problem for a fractional tumor growth model*, Mathematics **7**, 792 (2019).

[16] V. Cristini and J. Lowengrub, *Three-dimensional crystal growth-II: nonlinear simulation and control of the Mullins–Sekerka instability*, J. Cryst. Growth **266**, 552–567 (2004).

[17] S. Dai and Q. Du, *Computational studies of coarsening rates for the Cahn–Hilliard equation with phase-dependent diffusion mobility*, J. Comput. Phys. **310**, 85–108 (2016).

[18] M. Dehghan and M. Abbaszadeh, *The meshless local collocation method for solving multidimensional Cahn–Hilliard, Swift–Hohenberg and phase field crystal equations*, Eng. Anal. Bound. Elem. **78**, 49–64 (2017).

[19] Q. Du, C. Liu and X. Wang, *Simulating the deformation of vesicle membranes under elastic bending energy in three dimensions*, J. Comput. Phys. **212**, 757–777 (2006).

[20] A. Fakhari, M. Geier and D. Bolster, *A simple phase-field model for interface tracking in three dimensions*, Comput. Math. Appl. (2016).

[21] A. Fakhari, M. Geier and D. Bolster, *A simple phase-field model for interface tracking in*

three dimensions, Comput. Math. Appl. **78**, 1154–1165 (2019).

[22] A. Fasano and M. Primicerio, *Free boundary problems: theory and applications*, Pitman Advanced (1983).

[23] W. Feng, Z. Guan, J. Lowengrub, C. Wang, S. M. Wise and Y. Chen, *A uniquely solvable, energy stable numerical scheme for the functionalized Cahn–Hilliard equation and its convergence analysis*, J. Sci. Comput. **76**, 1938–1967 (2018).

[24] R. Gabbrielli, *Foam geometry and structural design of porous material*, Ph. D. thesis, University of Bath (2009).

[25] P. J. Gandy, S. Bardhan, A. L. Mackay and J. Klinowski, *Nodal surface approximations to the P, G, D and I-WP triply periodic minimal surfaces*, Chem. Phys. Lett. **336**, 187–195 (2001).

[26] H. Gomez, A. Reali and G. Sangalli, *Accurate, efficient, and (iso) geometrically flexible collocation methods for phase-field models*, J. Comput. Phys. **262**, 153–171 (2014).

[27] Z. Guo, P. Lin, J. Lowengrub and S. M. Wise, *Mass conservative and energy stable finite difference methods for the quasi-incompressible Navier–Stokes–Cahn–Hilliard system: Primitive variable and projection-type schemes*, Comput. Methods Appl. Mech. Eng. **326**, 144–174 (2017).

[28] D. Jeong and J. Kim, *Conservative Allen–Cahn–Navier–Stokes system for incompressible two-phase fluid flows*, Comput. Fluids **156**, 239–246 (2017).

[29] D. Jeong and J. Kim, *An explicit hybrid finite difference scheme for the Allen–Cahn equation*, J. Comput. Appl. Math. **340**, 247–255 (2018).

[30] D. Jeong and J. Kim, *Fast and accurate adaptive finite difference method for dendritic growth*, Comput. Phys. Commun. **236**, 95–103 (2019).

[31] V. Joshi and R. K. Jaiman, *A positivity preserving and conservative variational scheme for phase-field modeling of two-phase flows*, J. Comput. Phys. **360**, 137–166 (2018).

[32] K. B. Khattri and S. P. Pudasaini, *Channel flow simulation of a mixture with a full-dimensional generalized quasi two-phase model*, Math. Comput. Simul. **165**, 280–305 (2019).

[33] J. Langer, *Models of pattern formation in first-order phase transitions*, Directions in Condensed Matter Physics: Memorial Volume in Honor of Shang-Keng Ma pp. 165–186, World Scientific (1986).

[34] H. G. Lee and J. Kim, *Regularized Dirac delta functions for phase field models*, Int. J. Numer. Meth. Eng. **91**, 269–288 (2012).

[35] H. G. Lee and J. Kim, *A comparison study of the Boussinesq and the variable density models on buoyancy-driven flows*, J. Eng. Math. **75**, 15–27 (2012).

[36] Y. Li, H. G. Lee, D. Jeong and J. Kim, *An unconditionally stable hybrid numerical method for solving the Allen–Cahn equation*, Comput. Math. Appl. **60**, 1591–1606 (2010).

[37] V. Mohammadi and M. Dehghan, *Simulation of the phase field Cahn–Hilliard and tumor growth models via a numerical scheme: Element-free Galerkin method*, Comput. Methods Appl. Mech. Eng. **345**, 919–950 (2019).

[38] C.-L. Park, J. Gibbs, P. W. Voorhees and K. Thornton, *Coarsening of complex microstructures following spinodal decomposition*, Acta Mater. **132**, 13–24 (2017).

[39] J. Shin, D. Jeong, Y. Li, Y. Choi and J. Kim, *A hybrid numerical method for the phase-field model of fluid vesicles in three-dimensional space*, Int. J. Numer. Methods Fluids **78**, 63–75 (2015).

[40] J. Shin, H. G. Lee and J.-Y. Lee, *Convex splitting Runge–Kutta methods for phase-field models*, Comput. Math. Appl. **73**, 2388–2403 (2017).

[41] K.R. Elder, M. Katakowski, M. Haataja, M. Grant, *Modeling elasticity in crystal growth*,

Phys. Rev. Lett. **88**, 245701 (2002).

[42] K.R. Elder, M. Grant, *Modeling elastic and plastic deformations in nonequilibrium processing using phase field crystals*, Phys. Rev. E **70**, 051605 (2004).

[43] G. Tegze, G. Bansel, G.I. Tóth, T. Pusztai, Z. Fan, L. Gránásy, *Advanced operator splitting-based semi-implicit spectral method to solve the binary phase-field crystal equations with variable coefficients*, J. Comput. Phys. **228**, 1612–1623 (2009).

[44] R. Guo, Y. Xu, *A high order adaptive time-stepping strategy and local discontinuous Galerkin method for the modified phase field crystal equation*, Commun. Comput. Phys. **24**, 123–151 (2018).

[45] G. Demange, M. Chamaillard, H. Zapolsky, M. Lavrskyi, A. Vaugeois, L. Luneville, D. Simeone, R. Patte, *Generalization of the Fourier-spectral Eyre scheme for the phase-field equations: Application to self-assembly dynamics in materials*, Comput. Mater. Sci. **144**, 11–22 (2018).

[46] J. Swift and P. C. Hohenberg, *Hydrodynamic fluctuations at the convective instability*, Phys. Rev. A **15**, 319 (1977).

[47] N. Talat, B. Mavrič, V. Hatić, S. Bajt and B. Šarler, *Phase field simulation of Rayleigh–Taylor instability with a meshless method*, Eng. Anal. Bound. Elem. **87**, 78–89 (2018).

[48] R. Tavakoli, *Unconditionally energy stable time stepping scheme for Cahn–Morral equation: Application to multi-component spinodal decomposition and optimal space tiling*, J. Comput. Phys. **304**, 441–464 (2016).

[49] X. Wang, L. Ju and Q. Du, *Efficient and stable exponential time differencing Runge–Kutta methods for phase field elastic bending energy models*, J. Comput. Phys. **316**, 21–38 (2016).

[50] S. Wu and Y. Li, *Analysis of the Morley element for the Cahn–Hilliard equation and the Hele–Shaw flow*, arXiv preprint arXiv:1808.08581 (2018).

[51] S. Wu and J. Xu, *Multiphase Allen–Cahn and Cahn–Hilliard models and their discretizations with the effect of pairwise surface tensions*, J. Comput. Phys. **343**, 10–32 (2017).

[52] Y. Wu, M. Li, Q. Zhang and Y. Liu, *A retinex modulated piecewise constant variational model for image segmentation and bias correction*, Appl. Math. Model. **54**, 697–709 (2018).

[53] M. Xu, H. Guo and Q. Zou, *Hessian recovery based finite element methods for the Cahn–Hilliard equation*, J. Comput. Phys. **386**, 524–540 (2019).

[54] S.-D. Yang, H. G. Lee and J. Kim, *A phase-field approach for minimizing the area of triply periodic surfaces with volume constraint* Comput. Phys. Commun. **181**, 1037–1046 (2010).

[55] X. Yang, *Efficient linear, stabilized, second-order time marching schemes for an anisotropic phase field dendritic crystal growth model*, Comput. Methods Appl. Mech. Eng. **347**, 316–339 (2019).

[56] X. Yang and L. Ju, *Linear and unconditionally energy stable schemes for the binary fluid–surfactant phase field model* Comput. Methods Appl. Mech. Eng. **318**, 1005–1029 (2017).

[57] X. Yang, J. Zhao and X. He, *Linear, second order and unconditionally energy stable schemes for the viscous Cahn–Hilliard equation with hyperbolic relaxation using the invariant energy quadratization method*, J. Comput. Appl. Math. **343**, 80–97 (2018).

[58] K. Zhang, W.-S. H. Liu, et al., *Quantitatively inferring three mechanisms from the spatiotemporal patterns*, Mathematics **8**, 112 (2020).

[59] Z. Zhang and Z. Qiao, *An adaptive time-stepping strategy for the Cahn–Hilliard equation*, Commun. Comput. Phys. **11**, 1261–1278 (2012).

[60] W. Jiang, W. Bao, C. V. Thompson and D. J. Srolovitz, *Phase field approach for simulating solid-state dewetting problems*, Acta Mater. **60**, 5578-5592 (2012).

[61] Q. A. Huang, W. Jiang, J. Z. Yang, *An efficient and unconditionally energy stable scheme for simulating solid-state dewetting of thin films with isotropic surface energy*, Comput. Phys

26, 1444 (2019).

[62] M. Dziwnik, A. Münch, B. Wagner, *An anisotropic phase-field model for solid-state dewetting and its sharp-interface limit*, Nonlinearity **30**, 1465 (2017).

[63] W. Jiang, Q. Zhao, W. Bao, *Sharp-interface model for simulating solid-state dewetting in three dimensions*, SIAM J. Appl. Math. **80**, 1654–1677 (2020).